CELLULAR NEUROSCIENCE

An axon initial segment is required for temporal precision in action potential encoding by neuronal populations

Elinor Lazarov[1,2,3,4], Melanie Dannemeyer[3,5], Barbara Feulner[2,3,6], Jörg Enderlein[3,5], Michael J. Gutnick[1], Fred Wolf[2,3,6,7,8,9]*, Andreas Neef[2,3,6,7,8,9]*†

Central neurons initiate action potentials (APs) in the axon initial segment (AIS), a compartment characterized by a high concentration of voltage-dependent ion channels and specialized cytoskeletal anchoring proteins arranged in a regular nanoscale pattern. Although the AIS was a key evolutionary innovation in neurons, the functional benefits it confers are not clear. Using a mutation of the AIS cytoskeletal protein βIV-spectrin, we here establish an in vitro model of neurons with a perturbed AIS architecture that retains nanoscale order but loses the ability to maintain a high Na_V density. Combining experiments and simulations, we show that a high Na_V density in the AIS is not required for axonal AP initiation; it is, however, crucial for a high bandwidth of information encoding and AP timing precision. Our results provide the first experimental demonstration of axonal AP initiation without high axonal channel density and suggest that increasing the bandwidth of the neuronal code and, hence, the computational efficiency of network function, was a major benefit of the evolution of the AIS.

INTRODUCTION

Action potentials (APs) are the currency of information exchange between neurons in the brain. In central neurons, APs are initiated in the axon initial segment (AIS), a specialized compartment in the proximal axon. The AIS serves to separate the single output neurite—the axon—from the input, somatodendritic surface of the cell (*1*, *2*). It extends over tens of micrometers and features a regular nanoscale arrangement of the cytoskeletal proteins, βIV-spectrin, and AnkyrinG (AnkG) (*3*, *4*). These are only found in the AIS and nodes of Ranvier (*5*), and they control the creation and maintenance of the AIS (*1*, *6*–*9*). βIV-spectrin anchors AnkG to the cytoskeleton, and AnkG, in turn, binds voltage-dependent sodium channels (Na_V) and potassium channels (K_V). These specializations emerged early in evolution. Although ancestral state reconstruction indicates that a giant Ankyrin isoform was already present in early bilaterians (*10*), an AIS with characteristics similar to those of modern mammals first appeared in early chordates (*11*). First, Na_V and, later, K_V channels acquired specific AnkG binding sites (*12*), thereby making the AIS a locus of ion channel clustering. The conservation of the AIS over more than 400 million years of vertebrate evolution suggests that it confers substantial functional advantages on neurons and neural circuits. However, it is still not clear what these advantages are. The AIS establishes the proximal axon as the site of AP initiation by defining a single neuronal compartment where firing threshold is lowest. Because Na_V density is highest in the AIS (*13*–*15*), it would be natural to conclude that it is the high channel density that makes the AIS the AP initiation site. However, it is important to note that additional factors contribute to the low axonal firing threshold, including (i) a shifted voltage dependence of Na_V in the AIS, which favors activation at less depolarized voltages than in the soma (*14*, *16*, *17*), and (ii) the large electrotonic distance of the AIS from the capacitive load of the soma, which renders distal Na^+ influx more efficient for local membrane depolarization (*18*–*20*).

Because APs originate in the AIS, the electrical properties of this compartment determine the precise timing of the APs in response to fluctuating synaptic inputs. Thus, the molecular architecture of the AIS directly influences a key process in neuronal information processing: the encoding of synaptic input, received and processed in the dendrites, into AP output. Theoretical studies predict that encoding will be strongly influenced by the density and properties of Na_V channels (*21*, *22*).

In central neurons, Na_V density in the AIS is larger than it is in the soma (*13*, *14*). However, this does not necessarily mean that higher AIS channel density is prerequisite for axonal AP initiation; experimental evidence for this assertion is lacking. Computational simulations have been inconclusive. Some have indicated that axonal AP initiation is possible without any axon/soma gradient of channel density or channel properties (*18*, *20*), while others have posited the need for an axonal channel density that is dozens of times higher than the somatic channel density (*14*, *23*). Here, we experimentally address the following two questions crucial for understanding the benefits associated with AIS molecular architecture: (i) Is a high AIS channel density required for axonal AP initiation? and (ii) Is a high AIS channel density required for precisely timed AP generation?

To answer these questions experimentally, it is necessary to manipulate the ratio of axon/soma ion channel density. However, in so doing, it is important to maintain a proper ratio of Na_V and K_V channels, because it is this ratio that determines the excitability of the AIS (*9*, *24*). Therefore, a pharmacological approach using specific channel blockers would be a problematic experimental strategy because the balance can hardly be reliably controlled.

[1]Koret School of Veterinary Medicine, The Hebrew University of Jerusalem, P.O. Box 12, Rehovot 76100, Israel. [2]Max Planck Institute for Dynamics and Self-Organization, Am Faßberg 17, 37077 Göttingen, Germany. [3]Bernstein Center for Computational Neuroscience, Georg-August-University Göttingen, Am Faßberg 17, 37077 Göttingen, Germany. [4]University Medical Center Göttingen, Department of Pediatrics and Adolescent Medicine, Division of Pediatric Neurology, Robert Koch Str. 40, 37075 Göttingen, Germany. [5]III. Institute of Physics, Georg-August-University Göttingen, Friedrich Hund Pl. 1, 37077 Göttingen, Germany. [6]Max Planck Institute for Experimental Medicine, Hermann Rein St. 3, 37075 Göttingen, Germany. [7]Institute for Nonlinear Dynamics, Georg-August-University Göttingen, Friedrich Hund Pl. 1, 37077 Göttingen, Germany. [8]Center for Biostructural Imaging of Neurodegeneration, Von-Siebold-Straße 3A, 37075 Göttingen, Germany. [9]Campus Institute for Dynamics of Biological Networks, Hermann Rein St. 3, 37075 Göttingen, Germany.
*Corresponding author. Email: aneef@gwdg.de (A.N.); fred@nld.ds.mpg.de (F.W.)
†Lead contact.

Here, instead of pharmacology, we exploit a fundamental feature of AIS evolution: Na_V and K_V channels compete for a common binding region on the AnkG molecule (*24*). As a consequence, the ratio between Na_V and K_V channels is determined by their relative affinity to AnkG, while the overall channel density scales with the number of AnkG molecules. We reduced the number of AnkG-bound Na_V and $K_V7.2/3$ ion channels indirectly through a mutation of the AnkG anchor βIV-spectrin. The qv^{3J} mutation results in a scrambled C terminus because of a frame-shifting base insertion in the *Sptbn4* gene (Fig. 1C). It is the most conservative of all qv mutations and causes a mild, progressive phenotype that reflects a gradual change in properties of AIS and nodes of Ranvier over the course of postnatal development (*8*, *25*, *26*).

We now report that as qv^{3J} neurons mature, loss of βIV-spectrin results in loss of AnkG and a marked decrease of axonal Na_V density, while somatic Na_V density is not different from control. Despite this shift in Na_V density ratio, APs could still originate in the AIS. However, those APs were far less precisely timed, and the bandwidth of AP encoding was substantially reduced. We conclude that improved encoding of information by precisely locking APs to dynamic inputs constitutes a major consequence and benefit of high Na_V channel density in the AIS.

RESULTS

Modeling predicts that APs can initiate in the axon even with low axonal Na_V density

We first examined the predicted impact of reducing channel density at the AIS in multicompartment models of pyramidal neurons. An earlier study of such a model had found that APs initiate in the first node of Ranvier if the Na_V density in the AIS is lowered (*14*). Hallermann *et al.* (*27*) later devised an improved model of AP initiation, featuring updated K_V and Na_V channel models. Here, we used this latter model to study AP initiation as we reduce the ion channel density in the axon. We expect that removal of AnkG leads to a reduction of Na_V and K_V throughout the axon, but not the soma, where AnkG is not found. To mimic this, we used the same factor to reduce Na_V and K_V conductances in the axon and studied AP initiation in response to somatic current injections.

Even when the density of channels in the axon was lowered to the somatic level (Na conductance of 500 pS/μm^2), APs still initiated in the AIS (fig. S1, B and C). This is evident from a comparison of the voltages at the soma and axon during AP onset. In addition, the non-somatic initiation can also be deduced from the waveform of the AP

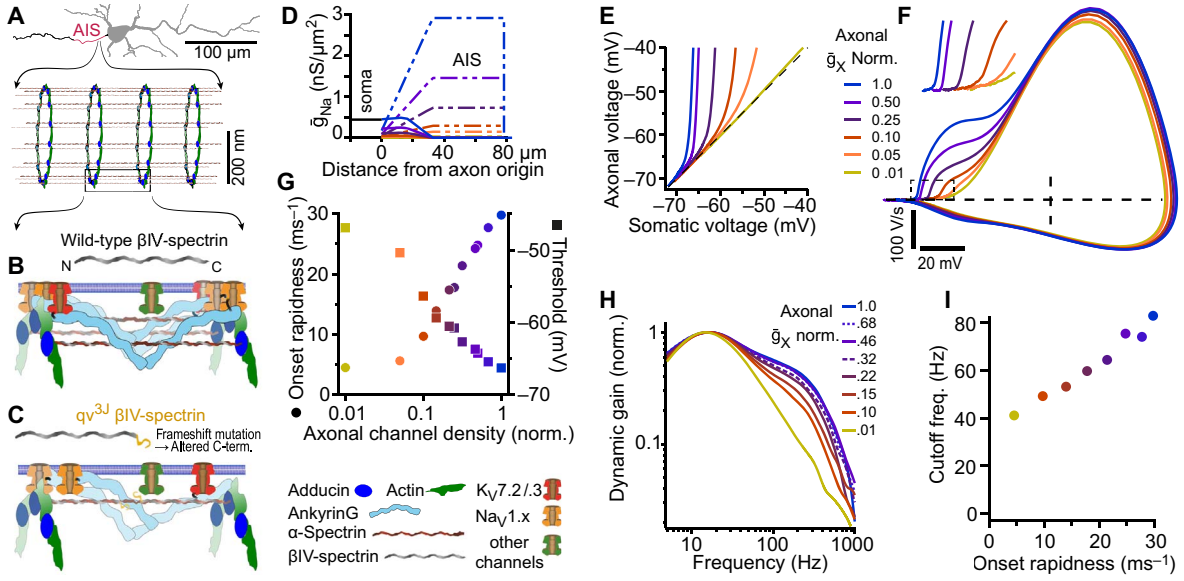

Fig. 1. Molecular down-regulation of AIS channel densities predicts axonal AP initiation with reduced timing precision. (**A**) The axon cytoskeleton in the AIS is highly regular. Tetramers of α- and β-spectrin serve as 190-nm-long spacers between rings of actin (green) and adducin (blue) (*3*, *55*). (**B**) Na_V and K_V channels are anchored to AnkG (light blue), which binds to βIV-spectrin and the lipid membrane (blue double layer). (**C**) The qv^{3J} mutation affects the very C-terminal portion of βIV-spectrin. We hypothesized that this might lead to a reduction in the number of intact tetramers, and hence, a reduction of AnkG and ion channels bound to it, while other channels (green) might be unaffected. The relative sizes of cytoskeletal proteins follow measures from electron microscopy (*66*). (**D**) We used a compacted version of a detailed biophysical model of pyramidal neurons (*27*) to study AP initiation under reduced AIS channel densities. The conductance densities of two Na channel subtypes in the model are displayed here (continuous lines, somatic; dashed lines, axonal channel variant with more hyperpolarized activation curve). All other conductances were also scaled down proportionally but are omitted here for clarity. Color code in (D) to (I) is identical, and steps are identical in (E) and (F). Note that for a 90% reduction (red), the somatic conductance density is higher than the axonal one; for 95% reduction (orange), the soma/axon density ratio is 3:1. (**E**) The voltages occurring during AP onset in the soma and 50 μm into the axon are plotted against each other. Even when axonal channel density is lower than somatic, the AP still started in the axon. Only for a 99% reduction of channel densities (soma/axon density ratio, 15:1), no sign of axonal initiation could be detected. (**F**) Phase plots, plotting the first temporal derivative of the somatic membrane voltage dV_m/dt against V_m, also showed a gradual change in the properties of the AP onset, as the axonal channel densities were reduced. Threshold was shifted by 20 mV, and the initial lateral current into the soma was less pronounced; in particular, the initial slope in the phase plot, called onset rapidness, decreased from 29.8 to 4.5 ms^{-1}. In contrast, the second phase of the AP waveform remained largely unchanged. Biphasic phase plots, indicating axonal initiation of APs, were obtained for density reduction as severe as 95%. (**G**) AP threshold (squares) and onset rapidness (circles) plotted against the degree of axonal channel density reduction. (**H**) Dynamic gain curves were calculated from 10^6 APs for each condition (see Materials and Methods). Dynamic gain curves showed a reduced bandwidth when the channel densities in the axonal compartment were reduced to 10% in six exponentially spaced steps. Loss of axonal initiation (yellow) reduced the bandwidth further. (**I**) Cutoff frequencies, defined as the frequencies at which the gain reaches 60% of maximum, drop as the axonal channel density is reduced, although for all densities probed, the AP starts in the soma, not in the axon.

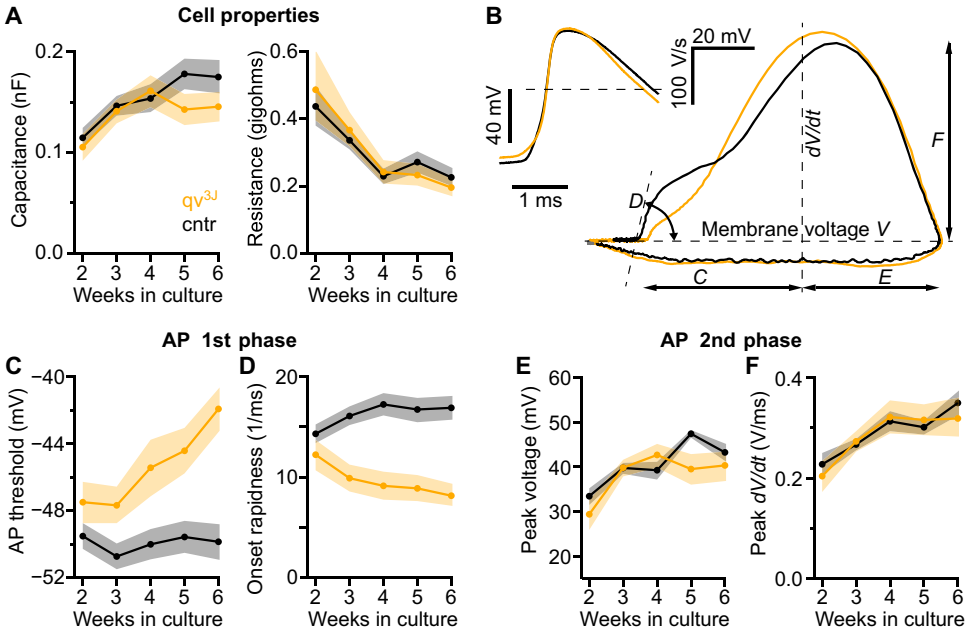

Fig. 2. APs of qv^{3J} mutants show depolarized threshold voltage and slower onset rapidness compared to control. (**A**) The qv^{3J} mutation has no effect on the cell membrane properties. Cell capacitance and resistance are similar in mutant and control littermates at different time points in culture development. (**B**) Representative phase plots (*dV*/*dt* versus *V*) from mature (>21 DIV) mutant (orange) and control (black) neurons, exemplifying the effect of the qv^{3J} mutation on the first, but not on the second, phase of the AP. Arrows and letters indicate the quantifications of AP waveform used in (C) to (F). (**C** and **D**) The quantifiers of the early AP phase, threshold and onset rapidness, increasingly diverged between qv^{3J} and control during development. The difference between mutants and controls was significant already after the second week in vitro. (**E** and **F**) The second phase of the AP was unaffected by the mutation. The peak voltage and peak rate of rise have similar values in both mutants and controls. (A and C to F) Number of cells (animals, litters) recorded at the five time points: n_{mutant} = 36 (10, 6), 44 (9, 6), 36 (6, 4), 47 (7, 5), and 43 (6, 4); $n_{control}$ = 70 (13, 11), 96 (12, 10), 78 (12, 9), 41 (7, 6), and 50 (6, 5). The mean is displayed, and shaded area represents the bootstrap 95% confidence interval.

in the soma. During the earliest phase of an AP, when the AIS is more depolarized than the soma, the somatodendritic membrane is charged by current flow from the AIS. This lateral current underlies the first phase of depolarization in the somatic AP waveform and can be seen in the phase plot as an abruptly rising, early transient (Figs. 1F and 2B and fig. S1A). Unlike the axonal voltage, this feature of the somatic AP waveform can be readily measured in electrophysiological experiments and can be used to identify the axonal origin of APs. When we decreased the channel density in the AIS, this first phase of AP depolarization changed, but the second phase was only minimally affected (fig. S1A). Furthermore, analysis of the somatic AP shape (see Materials and Methods) showed that AP threshold became more depolarized, and the initial slope of the phase plot, the onset rapidness, was reduced (fig. S1A). A similar pattern was observed for another detailed neuron model (*28*).

The results of our simulations are in line with an early theoretical study of the AP initiation site in a less complex model (*20*) that demonstrated AP initiation in the AIS, if soma and axon had the same density of ion channels and the dendrites were passive. If the axon can remain the locus of AP initiation even when ion channel densities are lower than normal, what then is the functional importance of the high density that is maintained by the specialized AIS proteins?

Modeling predicts that high axonal Na_V density improves the temporal precision of spike encoding

The family of qv mutations has been associated with an impaired AP timing precision. For example, various qv mutations are characterized by disruption of auditory-evoked brainstem potentials, which reflect the synchrony of AP generation across a neuronal population (*25*). To test timing precision in the model, we measured the model's dynamic gain (*29*–*35*). This function reveals how well the neuron can lock its APs to current fluctuations at different input frequencies in the presence of synaptic background activity. It expresses the susceptibility of the neuron's firing rate (in hertz per nanoampere) across a range of input frequencies. The higher the bandwidth of the dynamic gain, the more precisely APs are locked to brief fluctuations in the input current.

We next examined the relationship between encoding bandwidth and AIS channel density using a model that most closely matches AIS ion channel kinetics (*27*) and in which the AIS locus of AP initiation was maintained even in the absence of a soma/AIS gradient in channel density. By contrast with the few seconds of simulated time needed for AP shape analysis (fig. S1), calculation of a dynamic gain requires much more extensive simulation, as we collected 10^6 APs for each condition to calculate the gain curves with high precision. For a morphologically realistic model, this would require years of processor time. Therefore, we sped up the computation by compacting the model's morphology (see Materials and Methods). This modification did not alter the AP initiation properties (compare fig. S1 and Fig. 1). In the simulations, APs initiated in the AIS even when the channel densities in the axon were reduced by 95%, reversing the axon/soma gradient. Only a 99% reduction led to coincident initiation in AIS and soma, as evidenced in plots of axonal versus somatic voltage (Fig. 1E) and in the monophasic AP phase plot (Fig. 1F, yellow trace). As the axonal channel density was reduced, the shape of the early somatic AP waveform changed drastically. The threshold voltage shifted 20 mV to less negative values, and the onset rapidness dropped from 29.8 to 4.5 ms^{-1} (Fig. 1G).

Having assured that the compacted, computationally less demanding model behaves very similarly to the original model (*27*), we next used the compacted model to test whether the bandwidth of information encoding is affected by a reduced axonal channel density even if APs are still initiated in the AIS, that is, with axonal channel densities corresponding to a reduction of 0 to 90%. In addition, we tested the bandwidth for APs initiated in the soma, that is, the model with 99% reduction (Fig. 1, E to I, yellow). We stimulated the model with fluctuating currents (Materials and Methods), similar to published electrophysiological experiments that measured the dynamic gain (*31*). Mean and SD of the stimulus were adjusted to obtain a firing rate of 2 Hz and a coefficient of variation of the interspike intervals of 0.95 ± 0.03, that is, irregular firing. The correlation time of the stimulus was 35 ms. Following the established analysis procedure (*31*), we obtained dynamic gain curves for models with different axonal channel densities (Materials and Methods, Fig. 1H). To unambiguously define the bandwidth of the gain curves, we identified the cutoff frequency as the frequency at which the gain dropped to 60% of its maximal value. This cutoff frequency became smaller, meaning the precision of AP timing deteriorated as the axonal channel densities were reduced (Fig. 1I).

Our analysis suggests that the high axonal channel densities, created by a special molecular composition, are not important to achieve an axonal AP initiation locus, but instead are maintained to assure precise AP timing. Next, we set out to test whether these simulation results could be confirmed in patch-clamp experiments.

The initial but not the somatic phase of APs is affected by qv^{3J}

To test whether the simulation results were predictive of actual neuron function, we studied the neurons from mice homozygous for qv^{3J} (mutants) and control littermates throughout development, starting in the second week, just after the onset of AP firing, until the sixth week in vitro, using whole-cell patch clamp. During the first 2 weeks of this period, the membrane capacitance and conductance, assessed by short subthreshold current pulses, increased by about 50 and 100%, respectively (Fig. 2A). This reflects a growth of the somatodendritic compartment and occurred in both genotypes. We elicited APs by 100-ms current pulses, starting from a membrane voltage of −76 mV. The first AP evoked within a few milliseconds after current onset is analyzed, as shown in the phase-plane plot in Fig. 2B and explained in Materials and Methods. The early phase, associated with AP initiation, is characterized by the threshold voltage and the onset rapidness (Fig. 2, C and D). The second part of the AP upstroke is characterized by the peak rate of voltage rise and the peak voltage (Fig. 2, E and F).

We observed no effect of the qv^{3J} mutation on the passive cellular properties resistance and capacitance (Fig. 2A). Because these measures are mainly determined by the soma and proximal dendrites, we conclude that their growth is similar in mutants and controls. Next, we analyzed the peak rate of rise and the peak voltage. These features of the somatic AP waveform are selectively sensitive to the relation of somatodendritic size and somatic channel density (fig. S1, D to F), while they are insensitive to the axonal channel density (fig. S1A). Those measures are also hardly affected by the mutation (Fig. 2, E and F), since their 95% confidence intervals in mutants and controls overlap at almost all developmental stages. In contrast, the mutation showed a clear effect for AP properties that are sensitive to the axonal ion channels (fig. S1A). In qv^{3J} neurons, AP initiation requires a more depolarized somatic potential (Fig. 2C), and it progresses more slowly (Fig. 2D). These observations mirror the outcome of the simulations for reduced axonal channel densities (Fig. 1, F and G). These differences between the genotypes were small in the second week in culture but increased during the next 4 weeks, until the onset rapidness in mutants was only 48% of control (17 ± 1 ms^{-1} versus 8 ± 1 ms^{-1}) and the threshold potential differed by 8 mV (−50 ± 1 mV versus −42 ± 1 mV). The functional consequences of the qv^{3J} mutation seem to be limited to early AP stages, which occur in the AIS, while the somatic phase of depolarization seems unaffected. These observations and the comparison to the simulations (Fig. 1, F and G, and fig. S1, A and D to F) provide strong evidence for an unchanged development of somatodendritic compartments. However, the nature of whole-cell patch-clamp measurement does not directly provide the spatial resolution needed for more quantitative statements on the differences of axonal currents. To further investigate the effects of the qv^{3J} mutation with spatial resolution, we turned to immunocytochemistry.

βIV-spectrin is lost early on, and Na_V channels cannot be stabilized or recruited

In the AIS of control neurons, we observed, at all studied time points, strong signals from antibodies against AnkG, βIV-spectrin, and Na_V (pan-Na_V). All antibodies used displayed minimal background staining, which allowed a quantitative evaluation based on immunocytochemistry. In dSTORM (direct stochastic optical reconstruction microscopy) imaging, the same staining protocol permitted single-molecule detection (see Fig. 6, A to F). Example images for the fourth week are shown in Fig. 3A and fig. S3A. To quantify the spatial distribution of the immunosignal, we obtained the fluorescence intensity profile along the axon (Fig. 3, B and C, and fig. S3, B and C), starting at the soma or, in the case of axons branching off a dendrite, starting at the last branching point. As expected from the electrophysiology results in controls, the Na_V signal in the AIS increases over time, consistent with earlier reports (*8*). The fluorescence intensity of AnkG antibodies increased as well, similar to very recent observations (*36*). When we turned to neurons from littermates homozygous for qv^{3J}, we first asked whether βIV-spectrin is still present at the AIS. Only at the earliest time point studied, at 7 days in vitro (DIV), shortly after AIS assembly, we could detect a βIV-spectrin signal (fig. S3D). Even then, the fluorescence intensity was much weaker compared to the control group [mean ± SD of intensity along the first 30 μm of the AIS, 4.9 ± 1.2 (AU) in the mutants, n = 4 cells; 105.6 ± 58.8 (AU) in controls, n = 4 cells].

In contrast to the controls, qv^{3J} neurons failed to accumulate AnkG or Na_V in the AIS during development (Fig. 3B, orange profiles). Therefore, the density of Na_V at the AIS is lower in the mutant. A similar observation had been made for voltage-gated potassium channels (*37*). Given the low fluorescence signals in qv^{3J}, it was not always possible to unequivocally identify the axon as the one neurite that featured a stronger pan-Na_V immunostaining in the proximal part. The intensity profiles in Fig. 3 and fig. S3 represent the subset of qv^{3J} neurons where AIS identification succeeded. When we combined pan-Na_V and AnkG staining in a separate group of experiments, covering a shorter developmental period, we found that AnkG labeling allowed AIS identification even in cases where none of the neurites showed a distinctive pan-Na_V signal. We attribute this reliability of AnkG staining to the fact that, unlike pan-Na_V, AnkG antibodies did not label soma and dendrites. AnkG detectability might also be higher if AnkG antibodies have a higher affinity. This double staining allowed us to identify the axon even in some of the cells, where

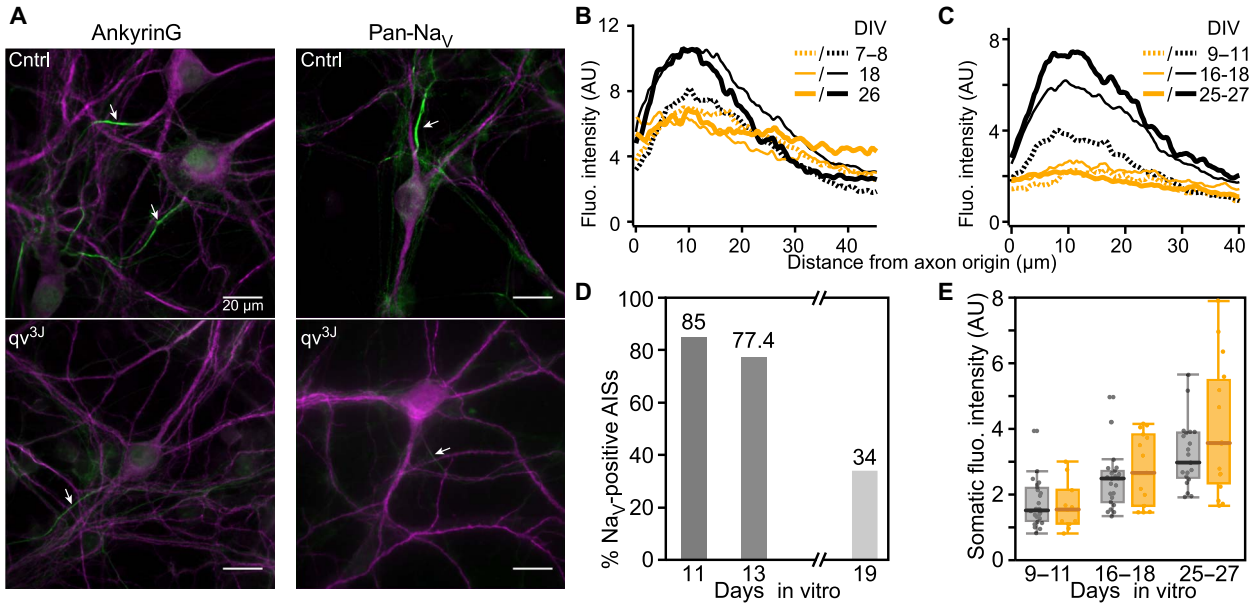

Fig. 3. Lower densities of Na_V channels and AnkG in the AIS of mature qv^{3J} mutant neurons. (**A**) Hippocampal neurons, 26 days in culture, from mutant and control animals were labeled with antibodies against MAP2 (magenta) and either Na_V channels (pan-Na_V) or AnkG (green); separate channels are shown in fig. S3F. (**B**) Profiles of AnkG immunosignal along the AIS, starting where it branches off the soma or a dendrite. Data from mutant are shown in orange, and data from control are shown in black at three developmental stages: 7 to 8 DIV, 18 DIV, and 26 DIV. n_{mutant} = 25 (2, 2), 17 (2, 2), and 14 (2, 2); $n_{control}$ = 26 (3, 2), 32 (3, 2), and 25 (4, 2). (**C**) As in (B), but for pan-Na_V immunolabeling: 9 to 11 DIV, 16 to 18 DIV, and 25 to 27 DIV. n_{mutant} = 13 (2, 2), 16 (2, 2), and 19 (3, 3); $n_{control}$ = 38 (4, 2), 83 (11, 4), and 32 (6, 3). In most mature mutant cells (>21 DIV), we could not identify an AIS based on its stronger pan-Na_V staining. The line profile shown here was obtained from the subset of neurons that still demonstrated an evident staining. To reduce cluttering, only the averages are shown in (B) and (C), and confidence intervals are shown in fig. S3. Note that AnkG and Na_V channel fluorescence intensity at the AIS of mutant cells remains low throughout maturation (orange curves) but increases in control cells (gray curves). (**D**) In a separate dataset, covering a smaller developmental period, cultures were double stained for AnkG and pan-Na_V. Here, axons could be identified by AnkG label even when no neurite showed enhanced pan-Na_V staining. Among the AnkG-positive axons, the fraction of pan-Na_V–positive AIS' decreased during development; n = 13 (1, 1), 84 (4, 3), and 35 (3, 2). (**E**) Average somatic pan-Na_V fluorescence intensity is similar in control and qv^{3J} mutant cells during development, suggesting that it is unaffected by the mutation. n_{mutant} = 11 (2, 2), 15 (2, 2), and 16 (2, 2); $n_{control}$ = 24 (5, 2), 23 (10, 4), and 21 (5, 2). AU, arbitrary units of camera signal, obtained under standardized conditions. Replication numbers refer to cells (animals, preps).

the Na_V label did not allow a clear AIS identification. In these cells, the Na_V label was imaged using dSTORM, a technique that allows detection and localization of individual fluorophores with extremely low background (see Fig. 6, A to F). If even under these conditions the outline of the AIS could not be identified in the pan-Na_V signal, the AIS was classified as Na_V negative. The fraction of AnkG-positive but Na_V-negative AIS grew over time (Fig. 3D), from 15% at 11 DIV to 66% at 19 DIV.

Remarkably, despite the strong reduction of Na_V immunolabeling at the AIS, the density in the soma appeared unaffected by the mutation (Fig. 3E). Therefore, electrophysiological assessment (Fig. 2, A, B, F, and G) and immunostaining both indicate that the structural and functional consequences of the qv^{3J} mutation are restricted to the AIS, while the structural and electrical maturation of the somatodendritic compartment is preserved.

To assess whether our immunocytochemical findings allow a semiquantitative characterization of Na_V densities, we compared them with the electrical signature of Na_V density. To this end, we recorded from 23 control neurons, which were then stained with pan-Na_V. When staining intensity in the AIS was plotted against the onset rapidness, a strong dependence was found (fig. S3E), similar to the relation between Na_V density and onset rapidness in the model (Fig. 1G, circles). Similarly, plotting staining intensity in soma against the peak of the second phase of the AP phase plot also revealed a high correlation (fig. S3E). In light of the selective sensitivity of these AP parameters (fig. S1, A and D to F), these results indicate that the pan-Na_V stain gave a quantitative estimate of the functional Na channels in the plasma membrane. Hence, our imaging results (Fig. 3E) show that the Na_V density in the somatic membrane was unchanged in those qv^{3J} neurons, where the AIS could be directly identified via the pan-Na_V antibody. Furthermore, the axonal density of Na_V in the mutant neurons at 25 to 27 DIV was about 75% reduced as compared to controls (Fig. 3C). This is only a lower bound of the actual reduction. As mentioned above, mutant neurons in which the Na_V label was too weak to identify the axon were excluded from this analysis.

The observed early loss of βIV-spectrin suggests that the frameshift mutation toward the C terminus removed an important interaction site that supports the retention of βIV-spectrin at the AIS. The subsequent loss of AnkG and Na_V could be simply a consequence of the disappearance of βIV-spectrin; however, it is unclear how the remaining AnkG and Na_V proteins are stabilized at the AIS when βIV-spectrin is already lost. Furthermore, the complete loss of this key structural protein raises the question of whether the regular nanostructure, which is thought to rely on spectrin tetramers, is also destroyed in qv^{3J}.

Combined patch clamp and immunostaining confirms axonal initiation despite low channel density

The results from electrophysiology and immunohistochemistry suggest that Na_V densities are reduced only in the axon, not in the soma.

Biphasic AP shapes, indicative of axonal AP initiation, occur at those developmental stages (fig. S2, 25 and 30 DIV) at which axonal Na_V immunolabeling becomes indistinguishable from somatic labeling (Fig. 3D). This already suggests that AP initiation can occur in axons with Na_V densities far below control levels. For a direct comparison, however, electrophysiology and immunolabeling need to be performed on the same preparations and cells. We thus set out to apply both techniques in the same sample to test most strictly whether AP initiation can occur in axons with Na_V densities far below control levels.

We recorded APs from 11 qv^{3J} mutant neurons, aged 14 to 28 DIV, and filled them with an Alexa dye through the patch pipette (Materials and Methods). Immediately afterward, the cultures were fixed and labeled with antibodies against AnkG and Na_V channels. Using this approach, we could identify the axon relying on the coincidence of AnkG staining and intracellular labeling via the patch pipette (see Fig. 4, fig. S4, and movie S1). In 4 of the 11 neurons, the AnkG was so weak that no identification was possible.

The staining and imaging protocols used here are identical to the ones used for Fig. 3. This allows a direct comparison of the intensities.

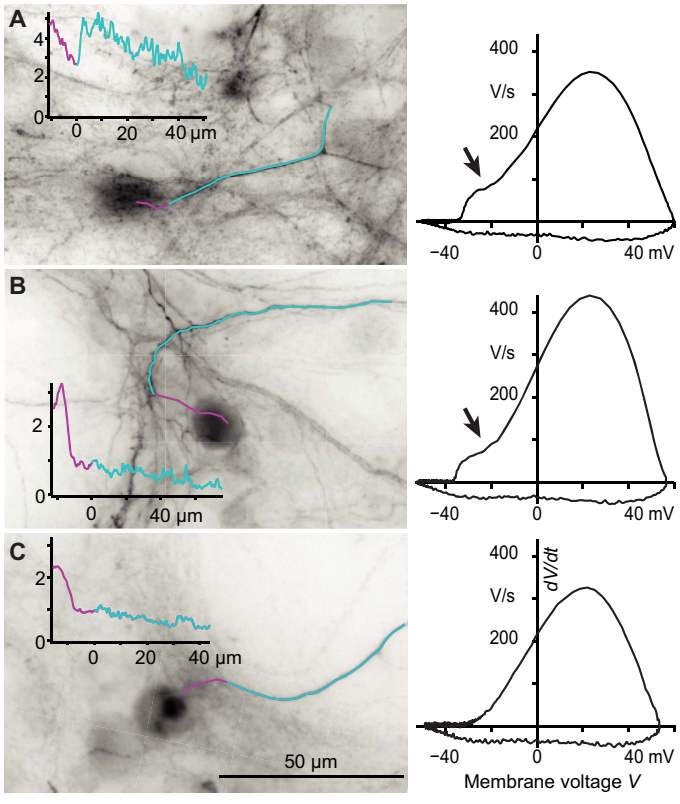

Fig. 4. Axonal initiation can occur even when channel density in the axon is lower than in the soma. Immunolabeling and phase plot analysis in the same mature (24 to 28 DIV) qv^{3J} neurons. (**A** and **B**) The biphasic phase plots demonstrate that APs were still initiated in the soma even when fluorescence intensity profiles indicate that the axonal Na_V channel density was either slightly larger than in the soma (A; 1.5 times higher) or even lower than in the soma (B). (**C**) In this neuron, APs appeared to initiate in the soma, as the phase plot shows no sign of any lateral current into the soma (compare Fig. 1B, 99% reduction). The immunostaining in the same neuron reveals an axonal pan-Na_V signal that is much lower than in the soma. The full dataset comprising more neurons is shown in fig. S4. Here, images were rotated for display purposes. A movie detailing the three fluorescence images used to identify the AIS and obtain the profile is in the Supplementary Materials.

The somatic pan-Na_V signal is in the range of 2 to 4, as reported in Fig. 3E. The axonal pan-Na_V signal of the filled neurons, however, is often lower than the typical axonal pan-Na_V signal in the previous dataset (see fig. S3C for average and 95% confidence intervals) due to the different identification criteria. The example in Fig. 4B has an axonal pan-Na_V signal between 0.5 and 1. This is less than half the average in Fig. 3C, but more importantly, this corresponds to an 85 to 95% reduction from the peak of the average intensity profile in control neurons (Fig. 3C). Despite the low axonal density, the APs in this neuron are initiating away from the soma, evident from the biphasic phase plot. One neuron with a similarly weak pan-Na_V signal lost the biphasic AP rise (Fig. 4C). This within-cell comparison of labeling and AP shape confirmed that APs can still initiate at the axon even when Na_V channel density is lower than the somatic density (Fig. 4, A and B).

Information encoding in qv^{3J} mutants

So far, our experimental results on the AP initiation in qv^{3J} mutants closely mirrored the behavior of the biophysical model under reduced axonal channel densities. We now set out to test the spike timing in qv^{3J} mutants and controls. In an analogy to the simulations, neurons were stimulated in whole-cell current clamp by injection of fluctuating currents with a correlation time of 35 ms, a value close to the typical membrane time constant (Fig. 2, A and B; Materials and Methods). The SD was adjusted to obtain a firing rate of approximately 2 Hz [control ν = 1.95 Hz (0.60), n = 11; qv^{3J} ν = 2.03 Hz (0.86), n = 16]. AP shapes and firing frequency showed no sign of adaptation throughout the 50-s-long stimulation episodes (Fig. 5A). Firing was highly irregular, and the local variation of interspike intervals (*38*) was on average lv = 1.05 (SD, 0.09) for controls and lv = 1.06 (SD, 0.08) for qv^{3J} mutants (Fig. 5G). Fast-spiking neurons, putative interneurons, had been excluded from analysis (fig. S5).

To quantify the bandwidth of frequencies that the cells can encode in their AP firing patterns, we followed the approach of Higgs and Spain (*31*) to calculate the dynamic gain. The overall shape of the dynamic gain was similar for both genotypes, and the dynamic gain curves peaked around input frequencies of 30 Hz and fell for higher frequencies (Fig. 5, C and F). However, in qv^{3J} mutants, this drop occurred at lower frequencies than it did in controls. This is evident from the nonoverlapping bootstrap confidence intervals for the two populations (Fig. 5F). To further characterize the difference, we compared the frequency at which the gain of individual cells drops to 60% of the peak value (Fig. 5C). This cutoff frequency was 36% smaller in qv^{3J} mutants (Fig. 5D). These results are in line with the changes observed in models when reducing the axonal channel densities (Fig. 1, H and I). This reduction in encoding bandwidth does not occur, because some of the APs fired in mutants were initiated in the soma. Instead, all the APs fired by a neuron in response to the fluctuating input share the same degree of biphasic onset (Fig. 5E), indicating an axonal initiation locus for every AP.

A simpler assessment of AP timing precision is conditional firing rate, computed for two AP sequences fired in response to the same fluctuating input (Fig. 5, G and H). As we used the same five stochastic stimuli for every neuron, we can characterize how precisely the population of neurons locks to the stimulus by computing the conditional firing rate for the two AP trains that a pair of neurons fired in response to the same input waveform. For threshold neuron models, the conditional firing rate under frozen noise and the dynamic gain function are closely related (*39*). A tight locking between stimulus

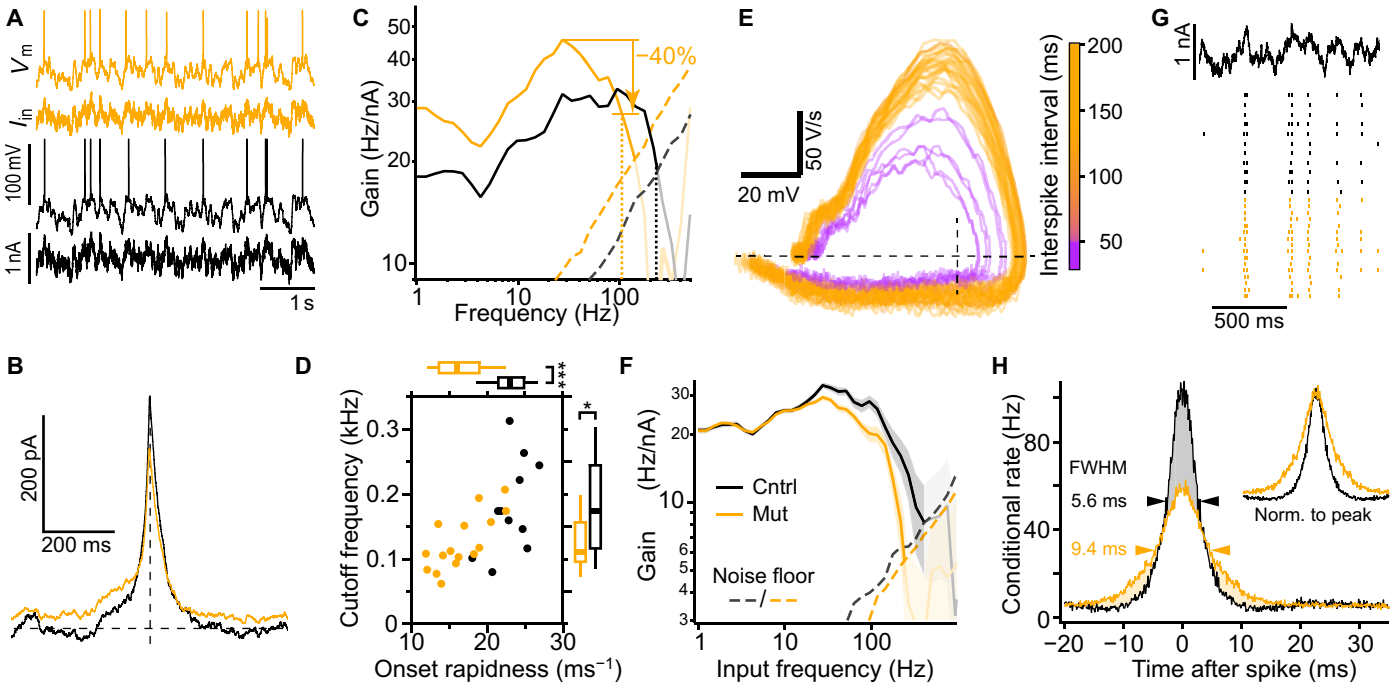

Fig. 5. Reduced precision of AP timing, bandwidth, and slower AP onset in qv^{3J} mutants. (**A**) Fluctuating input current (I_{in}, see Materials and Methods) and the resulting membrane voltage (V_m) of one control neuron (black) and one qv^{3J} mutant neuron (orange). (**B**) Spike-triggered average (STA) current of the two neurons from (A). (**C**) Dynamic gain for the two neurons (continuous lines) was considered significant up to the intersection with the noise floor (dashed lines). For calculations of gain and noise floor, see Materials and Methods. The cutoff frequency (dotted lines) for each gain curve was set as the point where the gain falls below 60% of its peak value. (**D**) Cutoff frequency plotted against AP onset rapidness (see Figs. 1I and 2D) for mutant and control cells. Box plots (median, quartiles, and 10th/90th percentiles) characterize the marginal distributions. The cutoff frequency was significantly lower in mutants (125.4 ± 10.6 Hz; mean ± SEM) than in controls (181.2 ± 21.8 Hz). *P = 0.0182, two-sided Student's t test. The AP onset rapidness was significantly smaller in mutants (16.5 ± 0.9 ms^{-1}) than in controls (23.1 ± 0.8 ms^{-1}). ***P = 0.000047, two-tailed Wilcoxon rank-sum test. (**E**) Phase plots of 30 randomly chosen APs from the mutant neuron in (A) to (C). Every AP is biphasic, indicating axonal initiation, even if the preceding interspike interval was less than 60 ms (color coded), resulting in a reduced overall availability of Na_V. (**F**) Average dynamic gain of mature (>21 DIV) neurons from qv^{3J} mutant mice and control littermates (wild type and heterozygous). Control: n = 11 cells (two mice from two litters); median age, 31 DIV; 5223 spikes. Mutant: n = 16 (four mice from four litters); median age, 29 DIV; 7909 spikes. The frequency response function of mutant neurons (orange) drops at lower frequency compared with control (black) neurons (average with 95% confidence interval; see Materials and Methods). Gain curves were considered significant until the intersection with the noise floor (dashed). (**G**) In response to frozen noise (top, stochastic stimulus 1; the average fluctuation amplitude used across all 27 cells is shown), 16 mutant and 11 control neurons fire APs locked to the stimulus. A 2-s-long interval with a slightly higher than average activity is shown. (**H**) Quantifying the precision of AP firing with the average conditional firing rate of pairs of neurons (see Materials and Methods), the qv^{3J} neurons show a broader peak, indicative of reduced precision. FWHM, full width at half maximum.

and AP initiation leads to little temporal jitter between the AP times of different neurons under the same stimulus (Fig. 5G), and hence, to a high and narrow conditional firing rate (Fig. 5H). Averaging across all neuron pairs, we found that for the qv^{3J} mutation, the average conditional firing rate has a smaller peak value and is broader: 9.4-ms full width at half maximum compared to 5.6 ms for the control neurons. Just as the reduced bandwidth of the dynamic gain, the broadening of the conditional firing rate reflects a less precise alignment between APs and the stimulus in the case of the qv^{3J} mutant.

The experimental results on the functional consequences of reduced axonal channel densities closely match the behavior of the biophysical model (Fig. 1), where all channel densities in the axon have been reduced, but no other changes occurred. Unlike the channels implemented in this model, ion channels in neurons operate in a context of other proteins and structural specializations. Most notably, Na_V and their anchoring proteins in the AIS are arranged in a highly regular nanostructure (*3*, *4*) of unknown functional relevance. To assess a potential relation of our functional findings to this nanostructure, we next studied whether qv^{3J} influenced the spatial order of axonal proteins.

AnkG and sodium channels retain their periodic organization in qv^{3J} AIS

Although it is not clear whether the regularity of the axonal cytoskeleton has any effect on electric signaling, one might argue that the functional consequences of a reduced channel density could be offset by other functional modifications, possibly related to an altered ion channel clustering. Beyond the question of AP initiation, the maintenance of AIS cytoskeleton in the qv^{3J} mutant is interesting in itself, because βIV-spectrin is thought to maintain the regular distance between actin rings (Fig. 1A).

We investigated the nanoscopic organization of AIS proteins using dSTORM, with Alexa Fluor 647–labeled secondary antibodies. As reported (*40*), the individual fluorophore localizations had a precision of 10 to 20 nm. In accordance with previous studies (*3*, *4*, *41*), we found that AnkG and Na_V are periodically spaced in the AIS, shown by a pronounced peak in the power spectrum of localization profiles at a spatial frequency of 1/190 nm (Fig. 6). Our data show that both AnkG and Na_V retain their periodic distribution in the AIS despite the complete loss of βIV-spectrin in the mutant. The periodicity of AnkG

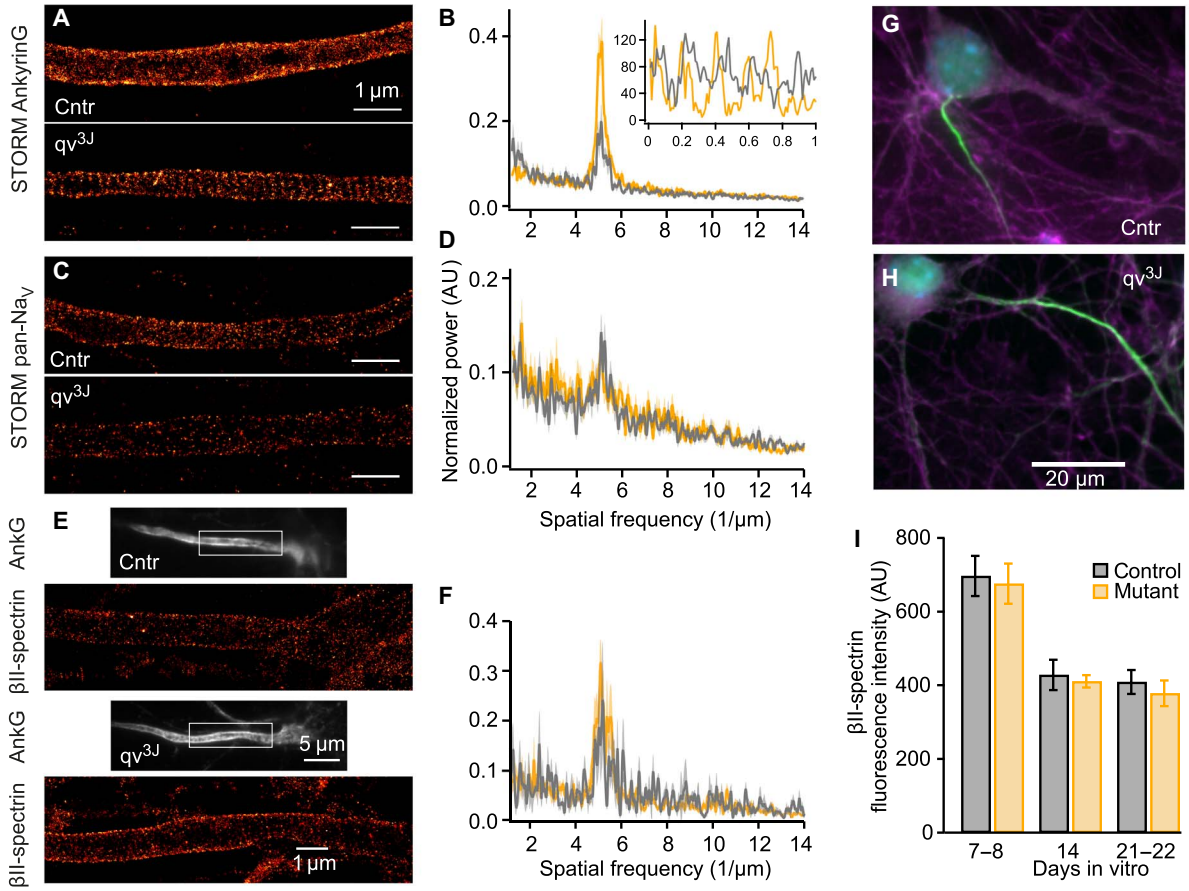

Fig. 6. The nanoscale spatial organization of AIS cytoskeleton in qv^{3J} is stabilized by βII-spectrin. (**A**) dSTORM images of AISs of control (top) and mutant (bottom) neurons, labeled with antibodies against AnkG (N terminus) at 13 to 14 DIV (for 10, 11, and 19 DIV, see fig. S6). Scale bars, 1 µm. (**B**) Power spectra analysis of AnkG immunofluorescence profile along the AIS of control, n = 28 (3, 3), and mutant, n = 53 (3, 3), demonstrating periodic pattern in both populations, with a periodic length of about 190 nm. Examples of individual immunofluorescence profiles along 1-µm segments are shown in the inset. (**C** and **D**) Same as (A) and (B) but with antibodies against Na_V, demonstrating periodic pattern with 190-nm periodicity in control and mutant (see fig. S6C for reduced periodicity in qv^{3J} at 19 DIV). $n_{control}$ = 33 (3, 2), n_{mutant} = 29 (4, 3). Error bars represent SEM. Replication numbers refer to cells (animals, preps). (**E**) Antibodies against AnkG (C terminus) label AIS (gray) in control and mutant cells (11 to 13 DIV). In the framed regions, βII-spectrin dSTORM imaging was performed (red). (**F**) Power spectra of βII-spectrin immunofluorescence profiles along the AIS show 190-nm periodicity in mutant, n = 14 (1, 1), and control cells, n = 25 (3, 2). βII-spectrin structural organization appears unaffected by the qv^{3J} mutation. Error bars represent SEM. (**G** and **H**) Cultures of 8 DIV control (G) and qv^{3J} mutant (H) neurons double labeled with antibodies against βII-spectrin (magenta) and AnkG (green) (C terminus) and 4′,6-diamidino-2-phenylindole (DAPI; nuclei, blue) (separate images in fig. S6). (**I**) βII-spectrin expression in control and qv^{3J} mutant neurons at three maturation stages. Fluorescence intensity of βII-spectrin label was averaged over 50.0 µm into the AIS. The results are similar for mutant and control and show no rescue effect for the βIV-spectrin deficiency. βII-spectrin expression was reduced with development. $n_{control}$ = 36 (3, 2), 22 (2, 1), and 27 (2, 2); n_{mutant} = 32 (2, 1), 11 (1, 1), and 22 (2, 2). Error bars represent SEM. Replication numbers refer to cells (animals, preps).

seemed even slightly more pronounced compared to control cells, possibly due to the reduced protein density. At 19 DIV, when the majority of mutant AIS do not display a discernible pan-Na_V labeling, the spectral power at 1/190 nm of the pan-Na_V label is reduced in the mutant (Fig. 6B, right). This breakdown of regularity is likely due to the labeling sparsity. Lower spatial frequencies are overrepresented, as would be expected when individual spots contain no pan-Na_V label at all. To allow identification of the AIS despite the very weak Na_V label, a double labeling with antibodies against AnkG was used, as in Fig. 3D.

βII-spectrin preserves cytoskeleton nanostructure in the qv^{3J} AIS

The presence and regular arrangement of AnkG and Na_V channels, weeks after βIV-spectrin had dropped under the detection limit, was surprising to us. In light of the crucial role that βIV-spectrin plays for the localization of AnkG and Na_V channels to the AIS (*7*, *26*, *42*, *43*), one might have expected a disintegration of the regular arrangement. On the basis of the observations by Zhong *et al.* (*4*), we speculated that a βII-spectrin could still be present in the mature AIS, thereby providing binding sites for AnkG. Antibodies against βII-spectrin labeled the AIS, as defined by the presence of AnkG, of neurons from mutant and control animals at all developmental stages tested. While the fluorescence intensity of βII-spectrin decreased by ~40% with development, it was still pronounced in mature neurons (>20 DIV) (Fig. 6, G to I). The intensity of βII-spectrin label in the AIS did not differ between qv^{3J} mutants and control, indicating that βII-spectrin is not up-regulated in the mutant to compensate for the complete loss of βIV-spectrin. In addition, βII-spectrin (labeled close to its C terminus) demonstrated a highly regular spacing of 190 nm (Fig. 6, E and F).

Together, these findings suggest that βII-spectrin constitutes part of the periodic actin-spectrin cytoskeleton of the mature AIS, to which AnkG and Na_V channels bind. The regularity of the remaining cytoskeleton seemed unaffected by the loss of βIV-spectrin in the qv^{3J} mutant. Apparently, the primary consequence is a reduction in the density of AnkG and the associated voltage-gated channels, rather than a loss of cytoskeleton regularity.

DISCUSSION

The qv^{3J} mutation in βIV-spectrin leads to a developmental loss of ion channel anchor proteins selectively in the AIS. By exploiting this experimental platform to disrupt the clustering of voltage-dependent ion channels in the AIS, we essentially partially rewind the tape of AIS evolution. By using a culture system, with its low fluorescence background, we are able to conclude that βIV-spectrin is absent from mutant AIS after 10 DIV. Nevertheless, single-molecule localization microscopy showed that AnkG and Na_V antibodies are still arrayed with the 190-nm periodicity characteristic of the spectrin/actin membrane undercoat. The regularity is probably maintained by βII-spectrin (*4*), which was present and not different in the AIS of mutants and controls. Levels of AnkG and Na_V did drop substantially during the second and third weeks in culture, and ultimately, neither could be labeled. The changes were restricted to the AIS because, over the same time span, Na_V staining in the soma, as well as soma-related electrophysiological measures, remained at control levels.

By determining the functional consequences of reduced axonal Na_V and K_V channel densities, we reveal the functional benefits afforded by the high AIS channel density. APs were initiated in the AIS, even when axonal Na_V channel density was reduced to about 10% of control, to a level that was lower than in the somatic membrane. This experimental finding unambiguously demonstrates that AP initiation in the AIS does not require the high local channel density. However, the precision of AP timing was substantially compromised when axonal channel density was reduced. Together, our results indicate that while clustering of ion channels at the AIS is not the reason AP initiation is shifted from the soma into the axon, it is required for tight temporal locking between initiation of APs and transient increases in input, as evidenced by the increase in the bandwidth of information encoding. These experimental findings and conclusions are completely substantiated by computational results obtained using the most refined models of pyramidal neurons (*27*, *28*).

Was precise AP timing a functional advantage for the early vertebrates that first evolved ion channel clustering in the proximal axon? Fossil data and molecular phylogeny suggest that the last common ancestor of all vertebrates was similar to present-day lamprey, and it is likely that it had camera-type eyes (*44*, *45*). Lampreys and mammals share basic neuronal infrastructure for complex behaviors, such as reward-based learning, visual processing for prey, conspecific and mate detection, and motor control (*46*–*48*). This suggests that the brains of stem vertebrates, whose neurons had an AIS, were complex and that they used multineuron populations to encode information. Our study reveals the unique features of the AIS, which, by promoting precise AP locking to transient changes in a continuously fluctuating input, may have created a substantial benefit in evolution of early vertebrates.

Our investigation is relevant to the many neurons in the mammalian central nervous system that operate in the fluctuation-driven regime. AP firing in these neurons is generally asynchronous and seemingly stochastic. For large populations of neurons, information about their shared input is encoded in the population's collective firing rate. We assessed the precision of this encoding in the time domain by comparing the responses to repeated presentations of the same fluctuating input and in the frequency domain by calculating the dynamic gain. Mutants performed much worse than controls in both assays. Recent theoretical studies showed that a larger dendritic compartment is associated with better encoding precision (*49*, *50*) and that properties of the AIS need not be a factor. We find that the passive properties of mutant and control neurons are not different, which implies that if there are differences in their dendritic trees, these are minimal, and that this cannot account for the observed marked decreased AP timing precision in the mutant. The strong reduction in the bandwidth of the dynamic gain seems to directly reflect the decrease in Na_V density as clusters of channels disassemble. Here, we directly demonstrate the dependence of dynamic gain on the physical properties of the axonal membrane at the site of AP initiation.

We are the first to show, on the level of individual neurons, that AP onset rapidness is correlated with the bandwidth of information encoding. This dependence of encoding capacity on the active properties of the AP initiation is consistent with earlier theoretical studies (*21*, *22*, *51*–*53*). Ilin *et al*. (*54*) used developmental changes in the AIS to probe the impact of its properties on encoding bandwidth and reported that older neurons have wider bandwidth and a faster AP onset. However, this result could be interpreted as reflecting the growth of somatodendritic size with age (*49*). In our study, the specific molecular manipulation of AIS channel density provides definitive experimental evidence for the direct impact of channel density on the temporal precision of AP encoding.

It is likely that our findings in culture are valid for neurons in vivo and in other experimental platforms. First, the AIS develops normally in hippocampal cultures, which are widely used for molecular studies of the AIS (*4*, *55*, *56*). Second, key functional properties of our control neurons, AP waveform and encoding bandwidth, are almost identical to those reported for pyramidal neurons in neocortical layer 2/3 and layer 5 in acute slices (*29*, *54*, *57*) and in vivo (*34*, *58*). Moreover, the biophysical model of AP initiation in a cortical pyramidal neuron (*27*) quantitatively reproduces our finding, suggesting that our findings are valid for neocortex.

We have shown that the functional benefit conferred by clustering of ion channels in the AIS is to promote precise encoding of information by populations of neurons. It is important to note that the properties of the AIS are not only altered by pathological conditions such as spectrinopathies (*59*); they may also be subject to modification as a component of neuronal plasticity under normal conditions (*60*–*63*). As yet, evidence for functional consequences of such plastic changes has been limited to measurement of changes in single-cell excitability. In light of our findings, it will be interesting to measure the effect of such changes on the bandwidth of information encoding.

MATERIALS AND METHODS

Cell culture

All animal experiments were performed in accordance with the guidelines for the welfare of experimental animals issued by the State Government of Lower Saxony, Germany, in compliance with European and National Institutes of Health guidelines (33.9-42502-04-13/1359 and 33.9-42502-04-13/1052). Hippocampi were isolated

from newborn (P0) qv^{3J} mice, collected in a serum-free Neurobasal-A medium (Life Technologies, 12349-015) with 100 mM Hepes buffer solution (Life Technologies, 15630-056), and digested with trypsin/EDTA (0.05%/0.02%, w/v; Biochrom) in phosphate-buffered saline (PBS) for 12 min at 37°C. The hippocampi were then transferred to Neurobasal-A medium, pipetted up and down for homogenization, and centrifuged for 2 min. Hippocampi from each newborn offspring were used to prepare a separate culture. For the dataset in fig. S3E, hippocampi from embryonic day 18 (E18) wild-type mice were pooled. For electrophysiology measurements and wide-field imaging, cells from the hippocampi of each newborn mouse were plated in one 8.8-cm^2 cell culture dish (Nunclon, 153066), on seven glass coverslips (Thermo Fisher Scientific, Menzel Gläser 10 mm #1), coated with poly-L-lysine (0.1 mg/ml; Sigma-Aldrich, P2636), in 2 ml of Neurobasal-A medium supplemented with 1:50 B27 (Life Technologies, 17504-044), 1:400 GlutaMAX (Life Technologies, 35050-038), and fibroblast growth factor (0.01 μg/ml; Life Technologies, 13256-029). For dSTORM imaging, the cells were seeded in four-well tissue culture chambers on cover glass (Sarstedt 94.61990.402), one hippocampus per well, in supplemented medium. Cultures were kept in an incubator at 37°C in a humidified atmosphere of 95% air and 5% CO_2. One-half of the culture medium was changed weekly with freshly prepared medium. Tail biopsies were used for genotyping and were afterward related with the corresponding culture.

Genotyping

Mice were genotyped by polymerase chain reaction (PCR) on tail biopsy samples using the following primers: forward, 5′-AGGCAGCGCCTTTGCTGCGTC-3′; reverse, 5′-TCCTGGTCACAGAGGTCCTTA-3′. PCR mix contained 1.0 μl of DNA, 0.2 μl of each primer, 0.4 μl of DreamTaq DNA Polymerase (Thermo Fisher Scientific, EP0703), and PCR buffer [containing tris-HCl (pH 8.8), ammonium sulfate (Sigma-Aldrich), $MgCl_2$ (Sigma-Aldrich), 2-mercaptoethanol (Merck), EDTA (pH 8.0) (Sigma-Aldrich), nucleoside triphosphates (2′-deoxyadenosine 5′-triphosphate, 2′-deoxycytidine 5′-triphosphate, 2′-deoxyguanosine 5′-triphosphate, and 3′-deoxythymidine 5′-triphosphate) (Promega), bovine serum albumin (BSA; Ambion—Life Technologies), and H_2O to a final volume of 20 μl]. PCR conditions were as follows: 3 min of initial denaturation at 94°C, followed by 36 cycles of 30-s denaturation at 94°C, 30-s annealing at 60°C, and 60-s elongation at 72°C. Final elongation was performed for 7 min at 72°C. Enzymatic digestion was performed with StyI (10 U/μl) (New England Biolabs, R0500S). The PCR product was separated by 3% gel electrophoresis (+/+ 600 bp, +/− 600 bp + 350 bp + 250 bp, −/− 350 bp + 250 bp).

Electrophysiology

Whole-cell recordings were performed in cells from cultures at different developmental stages in vitro. Extracellular medium contained 134 mM NaCl, 4 mM KCl, 2 mM $CaCl_2$, 1 mM $MgCl_2$, 10 mM Hepes, and 20 mM glucose (pH 7.4 with NaOH, 290 mOsm). Synaptic blockers against AMPA, γ-aminobutyric acid type A, and *N*-methyl-D-aspartate receptors [10 μM 2,3-dihydroxy-6-nitro-7-sulfamoylbenzo[f]quinoxaline, 50 μM picrotoxin, and 100 μM (2R)-amino-5-phosphonovaleric acid] were added to the medium and completely suppressed synaptic input and also abolished spontaneous activity in the culture. Patch pipettes were fabricated from PG10165-4 glass (World Precision Instruments) and contained K gluconate–based intracellular solution consisting of 136 mM K gluconate, 10 mM KCl, 5 mM NaCl, 0.1 mM EGTA, 1 mM MgATP, 0.3 mM NaGTP, 10 mM Hepes, and 5 mM phosphocreatine (pH 7.3 with KOH, 300 mOsm). Pipette resistance varied between 3 and 6 megohms, yielding access resistances between 5 and 15 megohms. In some experiments, 100 μM (final concentration) Alexa Fluor 568 hydrazide (sodium salt, Life Technologies, A-10437) was added to the intracellular solution (Fig. 6 and fig. S6). Whole-cell patch clamp was performed at room temperature (26°C) using an EPC10 amplifier controlled by Patchmaster (both HEKA Elektronik). The recordings were sampled at 100 KHz (step pulses) or 50 KHz (fluctuating input). Appropriate bridge and electrode capacitance compensation was applied. Using Patcher's Power Tools (F. Mendez and F. Würriehausen), the recordings were imported into Igor Pro (WaveMetrics) and analyzed with custom-written routines. Measurements were corrected for a calculated liquid junction potential (LJP) of 16 mV. All electrophysiological experiments were performed on cells from cultures derived from more than one embryo, from more than one litter. In fig. S2, data from a single litter are shown specifically to illustrate the clear difference between qv^{3J} and control on the background of the substantial variability within a single litter. Neurons were included when a complete dataset was available. For the data in Fig. 2, in rare instances, a single measure was not available; for example, when the estimation of cell capacitance was hampered by a particularly instable response to the hyperpolarizing test pulses. Provided that all other measures, for example, AP shape measures, were available, the neuron was included in those datasets in Fig. 2. This concerned at most three neurons (<5%) of any subgroup and, in total, only 2% of cells in Fig. 2 (see also the uploaded data file S1.

Current stimuli

The subthreshold membrane properties and the characteristics of the AP were obtained by injecting a series of 100-ms-long current steps with increasing amplitudes. Between stimuli, the neurons were held for 5 s at −76 mV (LJP corrected). For the data in Fig. 2, we analyzed the APs recorded for the smallest suprathreshold current for which an AP was generated within 10 ms after current onset.

Frequency response properties were investigated using input currents synthesized as Ornstein-Uhlenbeck (OU) noise with zero mean and a correlation time of 35 ms. The stimulus was applied for 50 s in five trials, separated by 60- to 90-s intervals, in which the cell was held at −76 mV. In each trial, the stimulus was generated with similar mean and SD but different random seed (i.e., different initial values of the internal state of the random number generator). The same five realizations of the noise, created by the same set of random seeds, were used for the different cells. The SD of the injected current was adjusted for each cell to achieve a firing rate of 2 to 3 Hz, while the DC component was adjusted to warrant a membrane potential fluctuating around −60 mV. For most cells, this DC component was no more than 20 pA.

Dynamic gain calculation

The frequency transfer function was calculated from responses to injected fluctuating current, using a method originally introduced by Bryant and Segundo (*64*) with modifications. AP time was registered when the somatic membrane voltage crossed 3 mV, which corresponds to the steepest point on the AP waveform. The STA current was calculated for each cell from ~600 spikes by averaging stimulus waveform in a temporal window of 500 ms before and after the spike. To improve signal-to-noise ratio, the STA was filtered in the frequency

domain using a Gaussian window $w(f')$, centered at frequency $f' = f$, with an SD of $f/2\pi$

$$w(f') = \frac{1}{\sqrt{2\pi}\cdot\left(\frac{f}{2\pi}\right)}\cdot\exp\left[-\frac{1}{2}\left(\frac{f'-f}{f/2\pi}\right)^2\right]$$

This averages out neighboring frequency components of similar amplitude but random phase, that is, noise. Deterministic frequency components with a phase that changes only mildly within the Gaussian window are not affected by this windowing. Thus

$$\mathrm{STA}_w(f) = \frac{\int \mathrm{STA}(f')\cdot w(f')\cdot df'}{\int w(f')\cdot df'}$$

If the train of APs is idealized as a discrete sequence of numbers with zero for empty samples and $1/dt$ for samples carrying an AP, then the product of the STA current and the firing rate ν equals the cross-correlation between input current and AP output. The frequency response function (or the dynamic gain), $G(f)$, was then calculated as the ratio between the Fourier transform of this cross-correlation $\widetilde{CC_{I\leftrightarrow AP}}$ and the Fourier transform of the autocorrelation of the input current $\widetilde{AC_I}$. The latter is equal to the power spectral density (PSD) of the input current, and for an OU process, the analytical expression of the PSD can replace the numerical autocorrelation

$$G(f) = \frac{|\mathrm{STA}_w(f)|\cdot\nu}{\mathrm{PSD}(f)} = \frac{\widetilde{CC_{I\leftrightarrow AP}}}{\widetilde{AC_I}}$$

$$\mathrm{PSD}(f) = \widetilde{AC_I} = \frac{4\tau_{\mathrm{corr}}\sigma^2}{1+(2\pi f\tau_{\mathrm{corr}})^2}$$

where σ is the SD of the input current and τ_{corr} is the correlation time of the noise.

To average the gain curves from N cells, we averaged the STA currents. To avoid overrepresentation of cells with a smaller input resistance, that is, cells that require a larger amplitude of current fluctuations, we weighted the STA curves: $\overline{\mathrm{STA}} = \frac{1}{N}\cdot\sum_{i=1}^{N}\mathrm{STA}_i\cdot\frac{\bar{\sigma}}{\sigma_i^2}$ with the average input variance $\bar{\sigma} = \frac{1}{N}\cdot\sum_{i=1}^{N}\sigma_i^2$. The average cross-correlation was obtained by multiplication with the average firing rate

$$\bar{\nu} = \frac{\sum_{i=1}^{N} n_i^{\mathrm{APs}}}{\sum_{i=1}^{N} T_i^{\mathrm{rec.}}}$$

$$\overline{G(f)} = \frac{|\overline{\mathrm{STA}}_w\cdot\bar{\nu}|}{\frac{4\tau_{\mathrm{corr}}\bar{\sigma}}{1+(2\pi f\tau_{\mathrm{corr}})^2}}$$

For each neuron and for the population average, we calculated the confidence intervals of the gain curve and the noise floor by balanced bootstrap. The confidence interval at a given frequency f' was defined by the 2.5th and 97.5th percentile of $G_{\mathrm{BST}}(f')$ for 200 bootstrap gain curves calculated from 200 random samples of actual AP times. The noise floor at a certain frequency is understood as 95th percentile of $G_{\mathrm{BST}}^{\mathrm{rnd}}(f')$ calculated not from measured but from random AP times. To obtain random AP times without changing the statistics of the AP time series, we applied a cyclic shift of the injected current by a random value larger than five correlation times. This results in a random triggered average of the input, which replaces the STA current in the calculations for $G_{\mathrm{BST}}^{\mathrm{rnd}}$. Neurons were excluded from the analysis if signs of nonstationarity in AP shape or other signs of cell instability, such as a drifting baseline potential, were detected.

Conditional firing rate

Each neuron in the dataset of dynamic gain and conditional firing rate analysis was stimulated with the same five stochastically changing current stimuli I^1 to I^5 (see the "Current stimuli" section), and only the fluctuation amplitude was adjusted between neurons to achieve firing rates of approximately 2 Hz. A given neuron m fires the AP sequences s_m^1 to s_m^5 in response to those stimuli. The conditional firing rate between neurons m and k is defined as the average over the conditional firing rates of the five trials

$$\nu_{\mathrm{cond}\ m,k}(\tau) = (\nu_m\cdot\nu_k)^{-1/2}\sum_{i=1}^{5}\left\langle s_m^i(\mathrm{t})\cdot s_k^i(t+\tau)\right\rangle$$

To obtain the average conditional firing rate of the neurons from control of mutant mice, we averaged

$$\nu_{\mathrm{cond}}(\tau) = \frac{2}{N_{\mathrm{cells}}\cdot(N_{\mathrm{cells}}-1)}\sum_{m=2}^{N_{\mathrm{cells}}}\sum_{k=1}^{m-1}\nu_{\mathrm{cond}\ m,k}(\tau)$$

AP characterization

The somatic AP waveform was characterized with the following set of parameters: The threshold voltage (V_{thresh}) was estimated as the value of the membrane potential when dV/dt crosses 25 V/s; the AP onset rapidness was calculated as the slope of the phase plot at the threshold voltage. The peak potential was the maximal value of V, and the peak rate of rise was the peak value of dV/dt. This rate of voltage change is proportional to the sum of all currents that charge the capacitance C, that is, $\frac{dV}{dt} = \frac{I}{C}$. At the peak of the second phase of AP depolarization, somatic sodium channels are the main current source charging the soma. Therefore, the peak rate of rise is indicative of the somatic sodium channel density. The relation is not exact, as lateral currents into the dendrites reduce somatic dV/dt. Great care was taken to properly compensate the fast capacitance because it has an influence on the shape of the phase plot.

Simulations

A multicompartment model, developed by Hallermann *et al.* (*27*) to capture the properties of AP generation in pyramidal neurons in brain slices, was used for the simulations of AP initiation and spike time precision (https://senselab.med.yale.edu/modeldb/ShowModel.cshtml?model=144526). The properties of all active conductances and their spatial distribution were left unchanged from the original model. To obtain the transfer functions for different axonal channel densities, many millions of seconds had to be simulated. To reduce the computational load, the model morphology was compacted: The basal dendrites and the apical dendritic branch and the initial axon were each represented by a single process with adjusted geometry, and two axon collaterals are branching off the main axon. Compacting the morphology did not alter the characteristics of the model for AP waveform or transfer function but greatly expedited simulations. For some simulations, we exchanged the somatic sodium channel model from Schmidt-Hieber and Bischofberger (*65*) against a similar model we had derived from our own measurements, the AP waveforms and transfer functions changed only marginally, and this version of the model was used for the results presented here.

To obtain the transfer function, the model is driven by somatic injection of a fluctuating current, derived from an OU process with a correlation time of 35 ms. The mean and SD of the process are chosen to obtain a firing rate of 2 Hz and a coefficient of variation of the interspike interval around 0.85. This reflects a fluctuation-driven state and closely matches the experimentally obtained firing statistics. Each simulation is 200 s long with sample interval of 0.025 ms; 250 such 200-s simulation are combined to obtain approximately 10^6 spikes for each set of axonal channel densities. AP time is set when the somatic voltage crosses +8 mV. From AP times and the input current, we calculate the STA input, which represents the cross-correlation of input and AP output. The transfer function TF is calculated as the ratio of the Fourier transformations of the cross-correlation (STA input) multiplied with the firing rate f and the autocorrelation of the input. The latter corresponds to the PSD of the input

$$\mathrm{TF} = \frac{\mathrm{FFT}(\mathrm{STA}) \cdot \nu}{\mathrm{PSD}_{\mathrm{OU}}}$$

Immunocytochemistry

Neurons were washed twice in PBS and fixed with 4% formaldehyde in PBS for 8 min at 4°C and then washed in PBS. Permeabilization was performed by 5-min incubation with 0.5% Triton X-100 in PBS, followed by 5-min incubation with 0.1% Tween in PBS. The cells were then incubated for 1.5 hours in 3% BSA and 0.1% Tween in PBS (blocking solution) and then in primary antibody diluted in blocking solution at 4°C overnight. After washing, secondary antibodies were diluted in blocking solution and applied for 45 min. For wide-field imaging, the coverslips were mounted on microscope slides using ProLong Gold antifade reagent with or without DAPI (Life Technologies, P36935 or P36930). For dSTORM imaging, the cells were post-fixed with 4% formaldehyde in PBS for 5 min, washed three times with PBS, and stored with PBS at 4°C.

The primary antibodies that were used in this study were as follows: mouse monoclonal anti-sodium channel (pan-Na_V) (1:900, clone K58/35; Sigma-Aldrich, S8809-1MG), goat polyclonal anti–βIV-spectrin antibody (1:200, OriGene, TA317365, targeting N-terminal sequence, amino acids 2 to 14), rabbit polyclonal anti–βIV-spectrin antibody (1:200, Atlas, HPA043370, targeting a centrally located sequence), rabbit polyclonal anti-AnkG antibody (1:200, Santa Cruz Biotechnology, sc-28561, targeting C-terminal sequence), mouse monoclonal anti-AnkG antibody (1:200, Santa Cruz Biotechnology, sc-12719, targeting N-terminal sequence), chicken polyclonal anti-Map2 (1:2000, Abcam, ab5392), and mouse monoclonal anti–βII-spectrin (1:200, Santa Cruz Biotechnology, sc-136074).

The following secondary antibodies were used (1:1000). For wide-field imaging, Alexa Fluor 488 goat anti-mouse (Life Technologies, A11029), Alexa Fluor 647 donkey anti-goat (Life Technologies, A21447), Alexa Fluor 488 goat anti-rabbit (Jackson ImmunoResearch 111-545-003), Alexa Fluor 647 goat anti-rabbit (Life Technologies, A21245), Alexa Fluor 647 goat anti-chicken (Life Technologies, A214469), and Alexa Fluor 488 donkey anti-chicken (Jackson ImmunoResearch 703-545-155) were used. For dSTORM imaging, Alexa Fluor 647 goat anti-mouse (Life Technologies, A21236) was used.

Wide-field imaging

Images were recorded using an inverted wide-field microscope (Olympus IX-71) equipped with a water-immersion objective lens [UPlanSApo, ×60 magnification, numerical aperture (NA) 1.2, Olympus]. Violet (emission maximum at 390 nm), cyan (emission maximum at 475 nm), yellow (emission maximum at 603 nm), and red (emission maximum at 634 nm) light-emitting diodes (LEDs) (Spectra X light engine, Lumencor) were used for excitation of DAPI, Alexa Fluor 488, Alexa Fluor 568, and Alexa Fluor 647, respectively. The fluorescence light was separated from the LED light with a dichroic beam splitter (59004bs, Chroma Technologies) and additional excitation filters (BLP01-405R, Semrock, for DAPI; FF01-520/35, Semrock, for Alexa Fluor 488; BLP01-594R, Semrock, for Alexa Fluor 568; and BLP01-635R, Semrock, for Alexa Fluor 647) before being imaged on an electron-multiplying charge-coupled device (EMCCD) camera (DU-897-CS0-BV, Andor) with an effective pixel size of 160 nm; the temperature of the detector is −50°C.

Images were analyzed using the image line profile operation (with a line width of 5 pixels) Igor Pro (WaveMetrics). Units refer to CCD pixel readout under strictly constant settings and parameters for immunostaining and imaging protocols within a dataset. AUs refer solely to the fact that the CCD's readout magnitude is arbitrary overall, but not within or between measurements. Specifically, it is not possible to compare fluorescence intensity units between different antibodies or detection protocols (STORM and widefield), but as the confidence intervals on repeated measurements with identical antibody batches and identical staining and imaging protocols show, there is good comparability within those measurements (fig. S3, B and C). Part of the imaging process is selection of suitable samples. We only used images from cells, where the entirety of the quantified axonal section is in the same focal plane. If the axon grows on top of other structures, the cell was rejected. Replication numbers for individual cells, cultures derived from individual embryos, and the number of litters were given in the figure legends where applicable.

dSTORM imaging

The imaging buffer used was 10 mM tris containing 100 mM cysteamine hydrochloride (Sigma-Aldrich, M6500), glucose oxidase (4.0 mg/ml; Sigma-Aldrich, G0543), catalase (0.57 mg/ml; Sigma-Aldrich, C40-100MG), and 10% glucose (Sigma-Aldrich, 49158-1KG-F). pH was adjusted with 0.5 M NaOH to pH 8.3 to 8.5. Chamber wells were completely filled with buffer and sealed bubble free (air free) by a regular coverslip. Images were recorded using an inverted total internal reflection fluorescence (TIRF) microscope (Olympus IX-71) equipped with an oil-immersion objective lens (Olympus, UApoN, ×100 magnification, NA 1.49, TIRF) and a 647-nm laser (PhoxX 647, 140 mW, Omicron Laserage, Germany). A quad-edge dichroic beam splitter (Di01-R405/488/561/635, Semrock) and a quad-band excitation filter (FF01-446/523/600/ 677, Semrock) were used to remove the laser light before imaging the fluorescence on an EMCCD camera cooled to −50°C (DU-885-CS0-#VP, Andor) with an effective pixel size of 80 nm. Raw movies typically contained 3000 to 4000 images recorded at 30 to 90 Hz. Images were analyzed using rapidSTORM and custom-written routines in Matlab.

SUPPLEMENTARY MATERIALS

Supplementary material for this article is available at http://advances.sciencemag.org/cgi/content/full/4/11/eaau8621/DC1

Fig. S1. Axonal AP initiation without channel density gradient in a model from Hallermann *et al.*

Fig. S2. APs from qv^{3J} mutant neurons lose their rapid onset with maturation—examples from one mutant mouse and one control mouse of the same litter.

Fig. S3. βIV-spectrin is absent in qv^{3J} mutants after the first week of development, and AnkG and pan-Na_V are significantly reduced.

Fig. S4. Immunolabeling and phase plane analysis of homozygous qv^{3J} mutant neurons at ages 14 to 28 DIV.
Fig. S5. Identification of putative fast-spiking neurons.
Fig. S6. Supplementary images of Fig. 6.
Movie S1. Figure 4 and fig. S4 display data from neurons that are filled during electrophysiological characterization, fixed, and immunolabeled for Na_V and AnkG.
Data File S1. Cell-by-cell characterization of AP waveform and passive properties.

REFERENCES AND NOTES

1. K. L. Hedstrom, Y. Ogawa, M. N. Rasband, AnkyrinG is required for maintenance of the axon initial segment and neuronal polarity. *J. Cell Biol.* **183**, 635–640 (2008).
2. M. N. Rasband, The axon initial segment and the maintenance of neuronal polarity. *Nat. Rev. Neurosci.* **11**, 552–562 (2010).
3. K. Xu, G. Zhong, X. Zhuang, Actin, spectrin, and associated proteins form a periodic cytoskeletal structure in axons. *Science* **339**, 452–456 (2013).
4. G. Zhong, J. He, R. Zhou, D. Lorenzo, H. P. Babcock, V. Bennett, X. Zhuang, Developmental mechanism of the periodic membrane skeleton in axons. *eLife* **3**, 10.7554/eLife.04581 (2014).
5. V. Bennett, A. J. Baines, Spectrin and ankyrin-based pathways: Metazoan inventions for integrating cells into tissues. *Physiol. Rev.* **81**, 1353–1392 (2001).
6. S. M. Jenkins, V. Bennett, Ankyrin-G coordinates assembly of the spectrin-based membrane skeleton, voltage-gated sodium channels, and L1 CAMs at Purkinje neuron initial segments. *J. Cell Biol.* **155**, 739–746 (2001).
7. M. Komada, P. Soriano, βIV-spectrin regulates sodium channel clustering through ankyrin-G at axon initial segments and nodes of Ranvier. *J. Cell Biol.* **156**, 337–348 (2002).
8. Y. Yang, Y. Ogawa, K. L. Hedstrom, M. N. Rasband, βIV spectrin is recruited to axon initial segments and nodes of Ranvier by ankyrinG. *J. Cell Biol.* **176**, 509–519 (2007).
9. D. Zhou, S. Lambert, P. L. Malen, S. Carpenter, L. M. Boland, V. Bennett, $Ankyrin_G$ is required for clustering of voltage-gated Na channels at axon initial segments and for normal action potential firing. *J. Cell Biol.* **143**, 1295–1304 (1998).
10. T. Jegla, M. M. Nguyen, C. Feng, D. J. Goetschius, E. Luna, D. B. van Rossum, B. Kamel, A. Pisupati, E. S. Milner, M. M. Rolls, Bilaterian giant ankyrins have a common evolutionary origin and play a conserved role in patterning the axon initial segment. *PLOS Genet.* **12**, e1006457 (2016).
11. P. M. Jenkins, N. Kim, S. L. Jones, W. C. Tseng, T. M. Svitkina, H. H. Yin, V. Bennett, Giant ankyrin-G: A critical innovation in vertebrate evolution of fast and integrated neuronal signaling. *Proc. Natl. Acad. Sci. U.S.A.* **112**, 957–964 (2015).
12. A. S. Hill, A. Nishino, K. Nakajo, G. Zhang, J. R. Fineman, M. E. Selzer, Y. Okamura, E. C. Cooper, Ion channel clustering at the axon initial segment and node of Ranvier evolved sequentially in early chordates. *PLOS Genet.* **4**, e1000317 (2008).
13. I. A. Fleidervish, N. Lasser-Ross, M. J. Gutnick, W. N. Ross, Na^+ imaging reveals little difference in action potential-evoked Na^+ influx between axon and soma. *Nat. Neurosci.* **13**, 852–860 (2010).
14. M. H. P. Kole, S. U. Ilschner, B. M. Kampa, S. R. Williams, P. C. Ruben, G. J. Stuart, Action potential generation requires a high sodium channel density in the axon initial segment. *Nat. Neurosci.* **11**, 178–186 (2008).
15. A. Lorincz, Z. Nusser, Molecular identity of dendritic voltage-gated sodium channels. *Science* **328**, 906–909 (2010).
16. C. M. Colbert, E. Pan, Ion channel properties underlying axonal action potential initiation in pyramidal neurons. *Nat. Neurosci.* **5**, 533–538 (2002).
17. W. Hu, C. Tian, T. Li, M. Yang, H. Hou, Y. Shu, Distinct contributions of $Na_v1.6$ and $Na_v1.2$ in action potential initiation and backpropagation. *Nat. Neurosci.* **12**, 996–1002 (2009).
18. G. Baranauskas, Y. David, I. A. Fleidervish, Spatial mismatch between the Na^+ flux and spike initiation in axon initial segment. *Proc. Natl. Acad. Sci. U.S.A.* **110**, 4051–4056 (2013).
19. R. Brette, Sharpness of spike initiation in neurons explained by compartmentalization. *PLOS Comput. Biol.* **9**, e1003338 (2013).
20. J. W. Moore, N. Stockbridge, M. Westerfield, On the site of impulse initiation in a neurone. *J. Physiol.* **336**, 301–311 (1983).
21. N. Fourcaud-Trocmé, D. Hansel, C. van Vreeswijk, N. Brunel, How spike generation mechanisms determine the neuronal response to fluctuating inputs. *J. Neurosci.* **23**, 11628–11640 (2003).
22. B. Naundorf, T. Geisel, F. Wolf, Action potential onset dynamics and the response speed of neuronal populations. *J. Comput. Neurosci.* **18**, 297–309 (2005).
23. Z. F. Mainen, J. Joerges, J. R. Huguenard, T. J. Sejnowski, A model of spike initiation in neocortical pyramidal neurons. *Neuron* **15**, 1427–1439 (1995).
24. M. Xu, E. C. Cooper, An ankyrin-G N-terminal gate and protein kinase CK2 dually regulate binding of voltage-gated sodium and KCNQ2/3 potassium channels. *J. Biol. Chem.* **290**, 16619–16632 (2015).
25. N. J. Parkinson, C. L. Olsson, J. L. Hallows, J. McKee-Johnson, B. P. Keogh, K. Noben-Trauth, S. G. Kujawa, B. L. Tempel, Mutant β-spectrin 4 causes auditory and motor neuropathies in quivering mice. *Nat. Genet.* **29**, 61–65 (2001).
26. Y. Yang, S. Lacas-Gervais, D. K. Morest, M. Solimena, M. N. Rasband, βIV spectrins are essential for membrane stability and the molecular organization of nodes of Ranvier. *J. Neurosci.* **24**, 7230–7240 (2004).
27. S. Hallermann, C. P. J. de Kock, G. J. Stuart, M. H. P. Kole, State and location dependence of action potential metabolic cost in cortical pyramidal neurons. *Nat. Neurosci.* **15**, 1007–1014 (2012).
28. E. Hay, F. Schürmann, H. Markram, I. Segev, Preserving axosomatic spiking features despite diverse dendritic morphology. *J. Neurophysiol.* **109**, 2972–2981 (2013).
29. C. Boucsein, T. Tetzlaff, R. Meier, A. Aertsen, B. Naundorf, Dynamical response properties of neocortical neuron ensembles: Multiplicative versus additive noise. *J. Neurosci.* **29**, 1006–1010 (2009).
30. M. Carandini, F. Mechler, C. S. Leonard, J. A. Movshon, Spike train encoding by regular-spiking cells of the visual cortex. *J. Neurophysiol.* **76**, 3425–3441 (1996).
31. M. H. Higgs, W. J. Spain, Conditional bursting enhances resonant firing in neocortical layer 2–3 pyramidal neurons. *J. Neurosci.* **29**, 1285–1299 (2009).
32. B. W. Knight, Dynamics of Encoding in a Population of Neurons. *J. Gen. Physiol.* **59**, 734–766 (1972).
33. G. Silberberg, M. Bethge, H. Markram, K. Pawelzik, M. Tsodyks, Dynamics of Population Rate Codes in Ensembles of Neocortical Neurons. *J. Neurophysiol.* **91**, 704–709 (2004).
34. T. Tchumatchenko, A. Malyshev, F. Wolf, M. Volgushev, Ultra-fast population encoding by cortical neurons. *J. Neurosci.* **31**, 12171–12179 (2011).
35. M. P. Touzel, F. Wolf, Complete firing-rate response of neurons with complex intrinsic dynamics. *PLOS Comput. Biol.* **11**, e1004636 (2015).
36. T. Yoshimura, S. R. Stevens, C. Leterrier, M. C. Stankewich, M. N. Rasband, Developmental changes in expression of βIV spectrin splice variants at axon initial segments and nodes of Ranvier. *Front. Cell. Neurosci.* **10**, 304 (2017).
37. J. J. Devaux, The C-terminal domain of βIV-spectrin is crucial for KCNQ2 aggregation and excitability at nodes of Ranvier. *J. Physiol.* **588**, 4719–4730 (2010).
38. S. Shinomoto, H. Kim, T. Shimokawa, N. Matsuno, S. Funahashi, K. Shima, I. Fujita, H. Tamura, T. Doi, K. Kawano, N. Inaba, K. Fukushima, S. Kurkin, K. Kurata, M. Taira, K.-I. Tsutsui, H. Komatsu, T. Ogawa, K. Koida, J. Tanji, K. Toyama, Relating neuronal firing patterns to functional differentiation of cerebral cortex. *PLOS Comput. Biol.* **5**, e1000433 (2009).
39. T. Tchumatchenko, F. Wolf, Representation of dynamical stimuli in populations of threshold neurons. *PLOS Comput. Biol.* **7**, e1002239 (2011).
40. S. van de Linde, A. Löschberger, T. Klein, M. Heidbreder, S. Wolter, M. Heilemann, M. Sauer, Direct stochastic optical reconstruction microscopy with standard fluorescent probes. *Nat. Protoc.* **6**, 991–1009 (2011).
41. C. Leterrier, J. Potier, G. Caillol, C. Debarnot, F. Rueda Boroni, B. Dargent, Nanoscale architecture of the axon initial segment reveals an organized and robust scaffold. *Cell Rep.* **13**, 2781–2793 (2015).
42. S. Lacas-Gervais, J. Guo, N. Strenzke, E. Scarfone, M. Kolpe, M. Jahkel, P. De Camilli, T. Moser, M. N. Rasband, M. Solimena, βIVΣ1 spectrin stabilizes the nodes of Ranvier and axon initial segments. *J. Cell Biol.* **166**, 983–990 (2004).
43. Y. Uemoto, S. Suzuki, N. Terada, N. Ohno, S. Ohno, S. Yamanaka, M. Komada, Specific Role of the Truncated βIV-Spectrin Σ6 in Sodium Channel Clustering at Axon Initial Segments and Nodes of Ranvier. *J. Biol. Chem.* **282**, 6548–6555 (2007).
44. S. E. Gabbott, P. C. J. Donoghue, R. S. Sansom, J. Vinther, A. Dolocan, M. A. Purnell, Pigmented anatomy in Carboniferous cyclostomes and the evolution of the vertebrate eye. *Proc. R. Soc. B* **283**, 20161151 (2016).
45. A. M. Heimberg, R. Cowper-Sal·lari, M. Sémon, P. C. J. Donoghue, K. J. Peterson, microRNAs reveal the interrelationships of hagfish, lampreys, and gnathostomes and the nature of the ancestral vertebrate. *Proc. Natl. Acad. Sci. U.S.A.* **107**, 19379–19383 (2010).
46. S. Grillner, A. von Twickel, B. Robertson, The blueprint of the vertebrate forebrain—With special reference to the habenulae. *Semin. Cell Dev. Biol.* **78**, 103–106 (2018).
47. V. N. Mikheev, J. Wanzenböck, A. F. Pasternak, Effects of predator-induced visual and olfactory cues on 0+ perch (*Perca fluviatilis* L.) foraging behaviour. *Ecol. Freshw. Fish.* **15**, 111–117 (2006).
48. B. Robertson, A. Kardamakis, L. Capantini, J. Pérez-Fernández, S. M. Suryanarayana, P. Wallén, M. Stephenson-Jones, S. Grillner, The lamprey blueprint of the mammalian nervous system. *Prog. Brain Res.* **212**, 337–349 (2014).
49. G. Eyal, H. D. Mansvelder, C. P. J. de Kock, I. Segev, Dendrites impact the encoding capabilities of the axon. *J. Neurosci.* **34**, 8063–8071 (2014).
50. S. Ostojic, G. Szapiro, E. Schwartz, B. Barbour, N. Brunel, V. Hakim, Neuronal morphology generates high-frequency firing resonance. *J. Neurosci.* **35**, 7056–7068 (2015).
51. M. Huang, M. Volgushev, F. Wolf, A small fraction of strongly cooperative sodium channels boosts neuronal encoding of high frequencies. *PLOS ONE* **7**, e37629 (2012).
52. B. Naundorf, F. Wolf, M. Volgushev, Unique features of action potential initiation in cortical neurons. *Nature* **440**, 1060–1063 (2006).

53. W. Wei, F. Wolf, Spike onset dynamics and response speed in neuronal populations. *Phys. Rev. Lett.* **106**, 088102 (2011).
54. V. Ilin, A. Malyshev, F. Wolf, M. Volgushev, Fast computations in cortical ensembles require rapid initiation of action potentials. *J. Neurosci.* **33**, 2281–2292 (2013).
55. C. Y.-M. Huang, C. Zhang, T. Szu-Yu Ho, J. Oses-Prieto, A. L. Burlingame, J. Lalonde, J. L. Noebels, C. Leterrier, M. N. Rasband, αII spectrin forms a periodic cytoskeleton at the axon initial segment and is required for nervous system function. *J. Neurosci.* **37**, 2112–2117 (2017).
56. M. R. Galiano, S. Jha, T. SzuYu Ho, C. Zhang, Y. Ogawa, K.-J. Chang, M. C. Stankewich, P. J. Mohler, M. N. Rasband, A distal axonal cytoskeleton forms an intra-axonal boundary that controls axon initial segment assembly. *Cell* **149**, 1125–1139 (2012).
57. H. Köndgen, C. Geisler, S. Fusi, X.-J. Wang, H.-R. Lüscher, M. Giugliano, The dynamical response properties of neocortical neurons to temporally modulated noisy inputs in vitro. *Cereb. Cortex* **18**, 2086–2097 (2008).
58. J. Doose, G. Doron, M. Brecht, B. Lindner, Noisy juxtacellular stimulation in vivo leads to reliable spiking and reveals high-frequency coding in single neurons. *J. Neurosci.* **36**, 11120–11132 (2016).
59. C.-C. Wang, X. R. Ortiz-González, S. W. Yum, S. M. Gill, A. White, E. Kelter, L. H. Seaver, S. Lee, G. Wiley, P. M. Gaffney, K. J. Wierenga, M. N. Rasband, βIV Spectrinopathies cause profound intellectual disability, congenital hypotonia, and motor axonal neuropathy. *Am. J. Hum. Genet.* **102**, 1158–1168 (2018).
60. M. S. Grubb, Y. Shu, H. Kuba, M. N. Rasband, V. C. Wimmer, K. J. Bender, Short- and long-term plasticity at the axon initial segment. *J. Neurosci.* **31**, 16049–16055 (2011).
61. M. S. Grubb, J. Burrone, Activity-dependent relocation of the axon initial segment fine-tunes neuronal excitability. *Nature* **465**, 1070–1074 (2010).
62. H. Kuba, Y. Oichi, H. Ohmori, Presynaptic activity regulates Na^+ channel distribution at the axon initial segment. *Nature* **465**, 1075–1078 (2010).
63. J. Lezmy, M. Lipinsky, Y. Khrapunsky, E. Patrich, L. Shalom, A. Peretz, I. A. Fleidervish, B. Attali, M-current inhibition rapidly induces a unique CK2-dependent plasticity of the axon initial segment. *Proc. Natl. Acad. Sci. U.S.A.* **114**, E10234–E10243 (2017).
64. H. L. Bryant, J. P. Segundo, Spike initiation by transmembrane current: A white-noise analysis. *J. Physiol.* **260**, 279–314 (1976).
65. C. Schmidt-Hieber, J. Bischofberger, Fast sodium channel gating supports localized and efficient axonal action potential initiation. *J. Neurosci.* **30**, 10233–10242 (2010).
66. S. L. Jones, F. Korobova, T. Svitkina, Axon initial segment cytoskeleton comprises a multiprotein submembranous coat containing sparse actin filaments. *J. Cell Biol.* **205**, 67–81 (2014).

Acknowledgments

Funding: This study was supported by the BMBF (01GQ0922), GIF (906-17.1/2006), VW foundation (ZN2632), BCCN (01GQ1005A, 01GQ1005B), BFNT (01GQ0811), DFG (CRC 889), and the Max Planck Society. **Author contributions:** Conceptualization: M.J.G., F.W., A.N., and E.L.; data curation: E.L. and M.D.; formal analysis: E.L., A.N., M.D., and B.F.; funding acquisition: M.J.G., F.W., A.N., and J.E.; investigation: E.L., M.D., and B.F.; methodology: A.N., B.F., J.E., F.W., and M.J.G.; software: A.N. and B.F.; supervision: A.N., J.E., F.W., and M.J.G.; validation: A.N. and E.L.; visualization: E.L., A.N., and M.D.; writing: E.L., A.N., M.J.G., and F.W. **Competing interests:** The authors declare that they have no competing interests. **Data and materials availability:** All data needed to evaluate the conclusions in the paper are present in the paper and/or the Supplementary Materials. Additional data related to this paper may be requested from the authors.

Submitted 22 July 2018
Accepted 26 October 2018
Published 28 November 2018
10.1126/sciadv.aau8621

Citation: E. Lazarov, M. Dannemeyer, B. Feulner, J. Enderlein, M. J. Gutnick, F. Wolf, A. Neef, An axon initial segment is required for temporal precision in action potential encoding by neuronal populations. *Sci. Adv.* **4**, eaau8621 (2018).